Unveiling hidden charge density waves in single-layer $NbSe_2$ by impurities

Fabrizio Cossu,[1,*] Ali G. Moghaddam,[2,†] Kyoo Kim,[3] Hassan A. Tahini,[4,5] Igor Di Marco,[1,6,7] Han-Woong Yeom,[7,8] and Alireza Akbari[1,3,7,2,‡]

[1]*Asia Pacific Center for Theoretical Physics, Pohang, Gyeongbuk 790-784, Korea*
[2]*Department of Physics, Institute for Advanced Studies in Basic Sciences (IASBS), Zanjan 45137-66731, Iran*
[3]*Max Planck POSTECH Center for Complex Phase Materials, POSTECH, Pohang 790-784, Korea*
[4]*Department of Applied Mathematics, Research School of Physics and Engineering, Australian National University, Canberra 0200, Australia*
[5]*Integrated Materials Design Centre (IMDC), School of Chemical Engineering, UNSW Australia, Sydney, NSW 2052, Australia*
[6]*Department of Physics and Astronomy, Uppsala University, Box 516, SE-75120, Uppsala, Sweden*
[7]*Department of Physics, POSTECH, Pohang, Gyeongbuk 790-784, Korea*
[8]*Institute for Basic Science Korea, Center for Artificial Low Dimensional Electronic Systems, Pohang 790784, South Korea*

(Received 1 August 2018; revised manuscript received 9 October 2018; published 14 November 2018)

We employ *ab initio* calculations to investigate the charge density waves in single-layer $NbSe_2$, and we explore how they are affected by transition metal atoms. Our calculations reproduce the observed orthorhombic phase in single-layer $NbSe_2$ in the clean limit, establishing the energy order between three different distorted structures, two consisting of triangular Nb-Nb clusters and a third, energetically unfavored, consisting of hexagonal Nb-Nb clusters. Such energy order, in agreement with known experimental work, is reversed by the adsorption of Co and Mn, which favor the formation of hexagonal Nb-Nb clusters; this CDW structure is indeed allowed from a symmetry point of view but hidden in pure single layers because it is at a higher energy. The other adsorbates, K and Ga, still favor one of the triangular Nb-Nb cluster, while suppressing the other. We report how the energy difference between such distorted structure varies with these adsorbates. Furthermore, transition metals induce magnetism and favor the reduction of the symmetry of the charge density distribution.

DOI: 10.1103/PhysRevB.98.195419

I. INTRODUCTION

Over the past decade, synthesis and exploration of atomically thin two-dimensional (2D) materials have almost revolutionized our common understandings of condensed matter systems and opened a new era in nanosciences [1–3]. In particular, 2D materials usually show drastically different electronic properties compared to their corresponding bulk structures composed of van der Waals (vdW) coupled atomic layers [4–6]. Transition metal dichalcogenides (TMDCs) are among vdW layered materials which show a wide range of interesting phenomena and applications due to the tunability of their electronic structures [7–10]. Moreover, they can host exotic phases, such as superconductivity (SC), charge density waves (CDW), and even topologically nontrivial states [11–15]. Strongly correlated phases in bulk TMDCs have been well studied for decades, and recent observations of CDWs and Ising SC [16] in few-layer films have revived interest in these materials [17–21].

Among TMDCs, $NbSe_2$ has been considered as a prototype material for investigation of CDW orders and SC [22,23]. Bulk 2H-$NbSe_2$ hosts a CDW phase with a 3×3 periodicity below 33 K which can coexist with an s-wave superconducting phase below 7 K [24–28], and it is known for its high magnetic anisotropy [29]. By reducing its thickness down to single layers, the SC weakens but still survives, whereas the CDW transition temperature increases [12,17,19]. The SC-CDW coexistence in $NbSe_2$ is due to a momentum dependent gap opening [27,30] accompanied by an electronic reconstruction over a wide energy range [31], leaving enough electronic states available for the superconducting transition. Such SC-CDW coexistence is maintained with charge doping, and their order parameters vary in the same fashion [20]. The origin of the CDWs has been intensively debated for some TMDCs, including $NbSe_2$, mostly because of controversies over the role of Fermi-surface nesting [32–39]. Nevertheless, in recent years theoretical and experimental evidences has been accumulated in support of momentum-dependent electron-phonon coupling as a key mechanism in the formation of CDWs [40–43]. Turning to 2D single layers, the lack of inversion symmetry, the disappearance of the coterminous of vdW interactions, and the interplay with many-body strong-correlation effects may lead to the aforementioned drastic changes [44–46].

On the other hand, the structure of CDWs in bulk and single-layer $NbSe_2$ is controversial [47–49]. While a recent detailed experimental work reported evidence of a 3×3 commensurate modulation of the crystal structure, the case of the single layer still needs to be clarified [40,48]. In addition, impurities or gate doping can play a major role on the CDW behavior. For example, long-range CDW phase coherence can be suppressed in $NbSe_2$ by a moderate percentage of Co or Mn intercalated at the surface [50], Na intercalated in a bilayer

*fabrizio.cossu@apctp.org
†agorbanz@iasbs.ac.ir
‡alireza@apctp.org

[51], and electron doping [20], whereas it can be increased by hole doping [20]. Besides, Bi adsorption can also lead to a transition to a stripe phase [52], previously observed in accidentally doped samples [53].

In this work, performing exhaustive first principle calculations, we reveal possible structures of CDWs, particularly at the presence of certain types of impurities. Among three different modulated structures, those two with triangular Nb-Nb clusters are found to be energetically favored in a clean $NbSe_2$ 2D sheet. These results are consistent with experimental evidence [47,48]. As a key finding we demonstrate that CDWs with hexagonal modulation can be established by adsorption of certain atoms such as Co and Mn. This type of CDW phase is in fact hidden in pristine $NbSe_2$ because it has a higher energy compared to triangularly-modulated CDWs. In addition, it is uncovered that the presence of the transition metal impurities induces magnetism and promotes modulated phases with reduced symmetry of the charge density distribution compared to pure CDW structures. Other types of metallic adatoms, namely K and Ga, allow the same ground state as pristine single-layer $NbSe_2$, but Ga also supports the hexagonally modulated structure. The current paper aims at steering future research towards a new interpretation of the experimental evidence on the effect of impurities [50,52,53] and represents an important contribution in the field of the interplay between CDWs and SC, as a recent work strongly points out [54].

This paper is organized as follows. In Sec. II, we will briefly introduce the computational method based on density functional theory which is used for investigation of CDW phases. Thereafter, we go through the results of *ab initio* calculations for CDWs in pristine $NbSe_2$, Sec. III, where the relaxed CDW structures and the profiles of charge densities are presented both in real space and in Fourier transformed form. The core of our work is found in Sec. IV, which shows the CDWs in the presence of various impurities. In particular, we show how the energy hierarchy of the CDWs can be different from the pristine system and a hidden order arises as a new ground state by adding Co or Mn adatoms. Finally, after a discussion over the results, the conclusions are presented in Sec. V.

II. COMPUTATIONAL DETAILS

Our results are obtained by means of density-functional theory (DFT). We employ the projected augmented wave (PAW) method with Perdew-Burke-Ernzerhof (PBE) pseudopotentials, as implemented in the Vienna *ab initio* simulation package (VASP) [55,56]. Accordingly, the exchange-correlation functional is treated in the generalized gradient approximation in the PBE parametrization [57,58]. The basis set consists of plane waves, with the explicit treatment of 13, 6, 9, 15, 9, and 13 valence electrons for Nb, Se, Co, Mn, K, and Ga states, respectively. As previously suggested [59], standard local and semilocal exchange-correlation functionals may not offer a proper description of the partially filled $3d$ and $4f$ shells of TM adatoms on 2D materials. Therefore, calculations involving Co and Mn are performed in the DFT $+ U$ approach, using the rotationally invariant formulation of Lichtenstein *et al.* [60]. As in Ref. [59], we use a generalized value of $U = 4.00$ eV and $J = 0.90$ eV for the $3d$ orbitals of both Co and Mn. Small variations of these parameters (within a reasonable range) are unlikely to change the physical picture outlined in the present paper. For sake of completeness we analyse this issue for Co adatoms in the Appendix. For all calculations, the cutoff energy of the plane waves is 400 eV, while the energy tolerance on the electronic loops for the relaxation and for the electronic properties are set to 10^{-6} eV and 10^{-7} eV, respectively; a conjugate gradient algorithm is employed for structural relaxation. Structures are considered relaxed when the forces on each atom are smaller than 2 meV/Å. The simulations are run in $3 \times 3 \times 1$, $6 \times 6 \times 1$, and $9 \times 9 \times 1$ replicas of the $NbSe_2$ single-layer unit cell. After convergence tests on the **k** meshes for the $3 \times 3 \times 1$ and $6 \times 6 \times 1$ replicas were performed, $15 \times 15 \times 1$, $7 \times 7 \times 1$, and $5 \times 5 \times 1$ grids of **k** points were used to sample their Brillouin zones for the total energy calculations; $11 \times 11 \times 1$ and $5 \times 5 \times 1$ **k** meshes were used for the partial charge density calculations in the $6 \times 6 \times 1$ and $9 \times 9 \times 1$ replicas, respectively; a $45 \times 45 \times 1$**k** mesh was used for the DOS calculations in the $3 \times 3 \times 1$ replica. In modeling metal adsorption on $NbSe_2$, the concentration of one adatom in a $6 \times 6 \times 1$ replica of the unit cell was adopted, corresponding to 0.0278 impurities/f.u., which allows for a description of a $3 \times 3 \times 1$ CDW while minimizing the interaction between impurities and their images. The adsorbates taken into account in the present study are Co, Mn, K, and Ga.

III. CDW PHASES IN PRISTINE SINGLE LAYERS

We begin with the study of the single-layer $NbSe_2$ in a $3 \times 3 \times 1$ supercell, which is the minimal size cell for a CDW in $NbSe_2$. Pristine single-layer $NbSe_2$ is known to be metallic, nonmagnetic, and hosts CDWs below 145 K [13,25,61]. Our models include three structures obtained according to existing work [17,47,48], which are shown in Fig. 1; the Nb atoms cluster in triangular patterns—see Figs. 1(a) and 1(b)—and hexagonal ones—see Fig. 1(c); the two triangular patterns differ by the position of the Se atoms with respect to the triangle composed by the Nb-Nb bonds; accordingly, the CDW structures are named T-U, T-C, and HX, respectively (T-U and T-C stand for triangle uncentered and triangle centered, whereas HX stands for hexagonal). The two structures T-U and T-C are related to each other by a mirror reflection of the Nb sublattice. It is also known that the Se-Se bond patterns (analogous to Nb-Nb bond patterns) accompany those of Nb-Nb [49]. The T-U and T-C CDWs differ for the Se-Se pattern, see the Appendix for details. Their total energies were compared in $3 \times 3 \times 1$ and $6 \times 6 \times 1$ replicas of the $NbSe_2$ unit cell and suggest that the formation of all of them is favored. The T-U is the lowest energy CDW structure; calculations in the $3 \times 3 \times 1$ supercell yield differences of 3.9 meV, 0.5 meV, and 1.3 meV/f.u. with respect to the undistorted structure, T-C and HX, respectively. In the $6 \times 6 \times 1$ supercell, slight changes are observed in the energy differences between the CDW structures: The T-U is favored by 0.4 meV and 1.1 meV over the T-C and HX, respectively; these differences are maintained for a $9 \times 9 \times 1$ supercell. The three CDW structures were recently investigated elsewhere on $3 \times 3 \times 1$ supercells [62]. Here, we demonstrate our agreement with Ref. [62], and

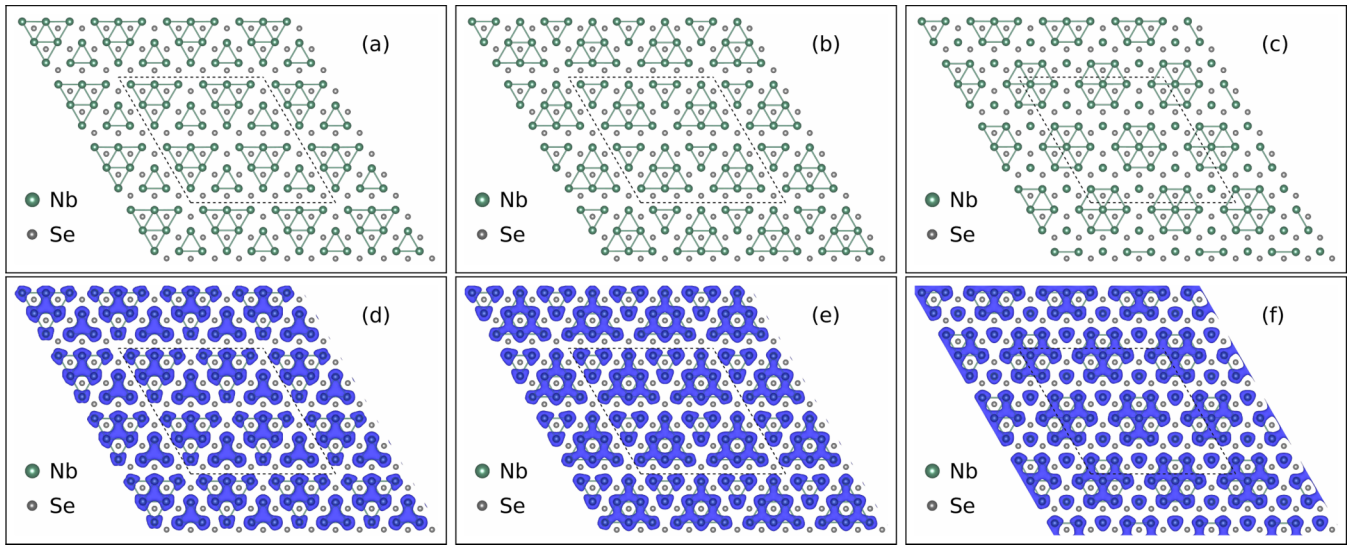

FIG. 1. First row: relaxed CDW structures for pristine $NbSe_2$ (top view): T-U (a), T-C (b), and HX (c) CDWs (see text for details). Second row: charge densities of the respective CDW structures. Volumetric data are represented as blue surfaces enclosing points whose electronic density is greater than or equal to 0.0075 electrons/Bohr^3. Atoms are represented by spheres, as illustrated in the legends (magnified); Nb-Nb bonds shorter than the equilibrium distance (3.45 Å) are represented by solid lines, in order to help visualizing the CDW structure pattern. Dashed lines mark the supercells borders.

we make use of the results for the pristine to compare the metal-adsorbed $NbSe_2$.

The effect of the CDW distortions on the density of states (DOS) is analyzed in the Appendix. For what concerns the electronic reconstruction following the CDW formation, our calculations are in agreement with the literature [40,63]. The charge distributions are computed integrating the charge density over the occupied Nb band (the band crossing Fermi level, see the Appendix) and they are shown in Fig. 1, second row. The integration over the whole occupied band simulates a topography retaining the symmetry of the Nb band only. The charge density clusters in patches, with different shape and patterns for each CDW; the lowest energy CDWs, T-U and T-C, have threefold symmetric patterns and the HX CDW has sixfold symmetric ones. The patches of T-U are on the vertices of a hexagon (with no element on the center), whereas those of T-C and HX are placed on the vertices and center of a larger hexagon.

The Fourier transform (FT) of the charge density distribution allows us to recognize more clearly the symmetry of the modulation patterns and trace their length scale. Due to the three-dimensional periodic boundary conditions, the three-dimensional data is originally computed as a function of the (h, k, l) Miller indices; the subset with $l = 0$ is analyzed to track modulations of the CDW charge distributions only along the plane. Thus, the FT is mapped as a function of h and k (k_x and k_y in the relative plots). The computed FT plots of the charge density distributions of the three CDW structures in pristine $NbSe_2$ are reported in Fig. 11, in Appendix A.

More significant information can be obtained by considering the difference between those plots and the FT plot of the charge density distribution of the nonmodulated structure, shown in Fig. 2. In these (and following) plots, the vertices of the large hexagon, at $|\mathbf{q}| = \frac{2\pi}{a}$, mark the position of the characteristic Bragg peaks, which are evident in Fig. 11.

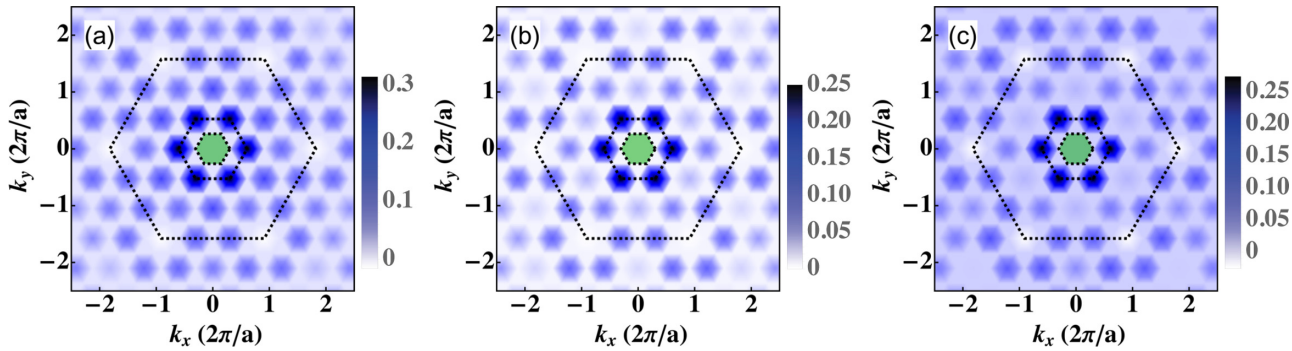

FIG. 2. Differences between the Fourier transform (FT) of the charge density distributions for the pristine CDW structures and the nonmodulated structure. The plots of T-U (a), T-C (b), and HX (c) CDWs charge density correspond to those in Fig. 1. The large dashed hexagon with vertices at $|\mathbf{q}| = \frac{2\pi}{a}$ (with $a = 3.45$ Å) marks the characteristic Bragg peaks; the medium size dashed hexagon with vertices at $|\mathbf{q}| = \frac{2\pi}{3a}$ marks the (shorter) CDW peaks; the small green shaded hexagon ($|\mathbf{q}| = \frac{2\pi}{6a}$) maps points beyond the supercell borders.

The vertices of the medium size hexagon, at $|\mathbf{q}| = \frac{2\pi}{3a}$, mark instead the position of the shorter peaks associated to the CDW. Both hexagons are emphasised with a dashed line, as a guide for the eye. The small green shaded hexagon, whose vertices are at $|\mathbf{q}| = \frac{2\pi}{6a}$, map points beyond the supercell borders, and thus are not meaningful. Due to the size of the supercell, the width of the spots denoting Bragg peaks or CDW peaks is large because different but close modulation frequencies cannot be resolved, even with a relatively dense **k** mesh. Figure 2 show the relative differences between the three CDWs and the nonmodulated structure. The CDW main peaks are not sensibly different from plot to plot, neither are satellite peaks at $(2/3)\Gamma\Gamma_1(\Gamma_1 = \Gamma + G)$ and at $(1/3)\Gamma_1\Gamma_1'$. However, a sizable satellite peak appears at K in the T-U CDW, but not (as large) in the T-C nor in the HX CDWs. Such configuration of peaks mirrors the configuration of the electronic patches in Fig. 1, which in the T-U (T-C and HX) are placed at the vertices of a small (large) hexagon, without (with) a central element. In fact, two different vectors map equivalent patterns in T-U. Naming the lattice vectors of the unit cell **a** and **b**, the mapping vectors are 3**a** (and equivalently 3**b**) and **a** + **b**; the latter does not map equivalent patches in T-C nor in HX.

IV. CDW PHASES IN THE PRESENCE OF IMPURITIES

Adsorption of the adsorbates Co, Mn, K, and Ga on a fully symmetric structure induces structural distortions breaking the symmetry of the $NbSe_2$ layer according to the site: The adsorption on the Nb site, hollow site, and Se site induces CDWs of HX type (i.e., having similar Nb-Nb distance patterns to the pristine HX), T-U type, and T-C type, respectively. By total energy calculations, the likelihood of the adsorption sites is analyzed. The energies for different adsorption sites of the investigated adatoms are reported in Table I. These results are consistent with those reported in a recent work on MoS_2 [64]. The preferred adsorption site is on top of a Nb atom for Co, K, Ga, and Mn. The competition between hollow site and Nb site is strong in the case of K (4 meV difference). The Se site remains the most unfavored for single atoms. However, it competes with Nb for larger molecules. In order to highlight this trend, we computed the energy difference for Co-$(OH)_2$, which can be considered as a prototype of a small molecule and a possible impurity. In the case of a single Co, the Nb site is preferred to the hollow site and Se site by 16 meV and 3551 meV, respectively; in the case of Co-$(OH)_2$, the corresponding energy differences are ∼670 meV and 166 meV, suggesting a hindrance to the Co-Se bonds and Co-Nb bonds or a decrease of the Co charge state and in turn of its coordination. In summary, single Co is preferably adsorbed on the Nb site, with the hollow site relatively close in energy; large molecules favor adsorption on the Se site and unfavor adsorption at the hollow site, a trend in line with combined theoretical and experimental results [65]. After establishing the preferred adsorption sites on the $NbSe_2$ nonmodulated structure for each adsorbate by total energy calculations, the adsorption on the different CDW structures is modelled (it involves different inequivalent adsorption sites due to the lower symmetry).

TABLE I. Energetics and magnetism for M|$NbSe_2$ (M = Co, K, Ga, Mn). Energy differences are computed with respect to the lowest configuration and are expressed in meV. Magnetic moments are expressed in μ_B.

		ΔE	μ^{TM}	μ_{tot}
Co	hollow	16	1.9	2.2
	top Nb	0	1.9	2.0
	top Se	3551	2.0	3.4
Mn	hollow	91	4.4	5.8
	top Nb	0	4.4	4.3
	top Se	1291	4.9	4.1
K	hollow	4	0.0	5.9
	top Nb	0	0.0	0.0
	top Se	241	0.0	1.2
Ga	hollow	183	0.0	5.9
	top Nb	0	0.0	0.0
	top Se	605	0.0	0.2

A. Adsorption of Co

Upon adsorption of Co, the energy and state of CDWs are modified. In general, the solutions are a combination of the states found in the pristine system. Pure solutions of the T-U CDW are found and are referred to as such in the remainder. The HX CDW solutions are found in mixed states or pure states; those with lowest energy are grouped according to the symmetry of their structures and charge densities, and named HX-S and HX-A, for symmetric and asymmetric ones, respectively. The T-C CDW solutions are found only mixed (with the HX-A CDW). The HX-S, HX-A, and T-U CDWs structures are shown in Figs. 3(a), 3(b) and 3(c), respectively. The HX-S features the characteristic hexagonal patches of the pristine HX CDW together with a trifold symmetric star of Nb-Nb bonds, compare Figs. 3(a) and 1(c). Their charge density distributions are not remarkably different from their pristine counterparts, compare Figs. 3(d) and 1(f). The flatness of the (multidimensional) potential energy surface allows adsorption on different sites of the underlying CDW structure to give different solutions. As Table II reports, the HX-A CDW results from the relaxation of the adsorption of Co on the vertex of the large triangle of a T-C CDW structure, compare Fig. 1(b), and a mixing between the T-C and the HX CDWs occurs. The patches in the charge density distribution, Fig. 3(e), recall those in both the pristine T-U and the pristine T-C, Figs. 1(e) and 1(f), supporting the previous observation. Finally, the structure and charge density distribution of the T-U solution are virtually identical to those in the pristine T-U CDW, with minor differences around the adsorption site, compare Figs. 3(f) and 1(a).

The magnetic density distributions exhibit antiferromagnetic coupling between Co and Nb in the occupied Nb band; moreover the magnetization around Co in that energy range is opposite to the total magnetization on Co, compare Fig. 4, first row, with Table III. The magnetic moment on Co (value integrated over all the occupied states) is around 2.0 μ_B for every CDW, and the total magnetization over the whole $NbSe_2$ layer vanishes. The same observation is valid for Mn, see Table III, and the discussion in the Appendix. The modulation

TABLE II. Energetics for the CDWs in M|$NbSe_2$ (M = Co, Mn, K, Ga); the energy for each column (adsorbate) is given as differences with respect to the ground state. Different position and resulting structure are possible for each metal M adsorbed on a CDW; we report those which evolve to structures relatively close in energy to the ground state, mentioning the type of structure, when it is similar to one of the three pristine CDWs, as well as the energy difference. The difference in energy in the 9×9 supercell (1 Co) is 0.3 meV/f.u. in favor of the HX CDW.

pristine		Co		Mn		K		Ga	
T-U	(0.0)	T-U	(0.7)	T-U	(1.5)	T-Uh	(0.0)	T-U	(0.0)
		T-U	(2.6)			T-UN	(0.2)		
T-C	(0.4)	HX-A	(0.0)	HX-A	(0.0)	T-CN	(1.5)	HX-A	(0.1)
						T-Ch	(1.3)		
HX	(1.1)	HX-S	(0.0)	HX-S	(0.0)	HX-S	(0.7)	HX-S	(0.0)
		HX-A	(0.0)	HX-A	(0.0)				

of the magnetization density in the HX-A CDW is larger than that in the HX-S (and that in T-U) CDW, compare Figs. 4(a) and 4(b), first row, suggesting that larger mixing of different CDWs supports the formation of a spin density wave (SDW). Moreover, a different modulation of the magnetization densities of Co|$NbSe_2$ T-U with Co at different adsorption CDW sites is observed, compare Figs. 4(c) and 4(d). These two structures are at the same energy, suggesting that a magnetic order transition is still incipient. The magnetization data obtained by a site-by-site analysis point to a ferromagnetic coupling, in agreement with Ref. [66], where an incipient magnetic transition is achieved by tensile strain.

The variation of the charge modulation can be analyzed looking at the difference in the charge density distribution between Co|$NbSe_2$ CDWs and the pristine CDWs in the direct space, see Fig. 3. In these plots, blue (red) lobes denote injection (depletion) of charge with respect to the pristine CDW charge distribution. The adsorption of Co modifies the T-U CDW only in the neighborhood of the adsorption site, see Fig. 5(a), as expected from Fig. 3(f); charge depletion (injection) occurs out-of-plane (in-plane) in correspondence to the Nb at the adsorption site and in a more complex pattern on the surrounding Nb atoms; in general, red lobes point towards the adsorbate. The charge difference between the HX-A and the T-U CDWs features a constant charge difference—due to the misalignment between the two charge densities (in $NbSe_2$ and Co|$NbSe_2$)—and an enhancement of in-plane modulations identified by the isolated blue lobes in Fig. 5(b); these may be more relevant in comparison to the out-of-plane modulations represented by the out-of-plane red lobes on isolated Nb atoms in Fig. 5(c), which refer to Mn-adsorbed $NbSe_2$.

Eliminating charge displacements (due to the different adsorption sites) helps analyzing the symmetry of the charge distribution. In analogy to what was done for the pristine case (Fig. 2), we do not show the FT plots of the charge density distributions directly. Instead, we focus on the differences between these plots and the FT plot obtained for the T-U CDW in the pristine case. In order to identify variations in the CDW signal, the marks of Bragg peaks, CDW peaks, and the region corresponding to points in the direct space beyond the supercell size are used in agreement with Fig. 2.

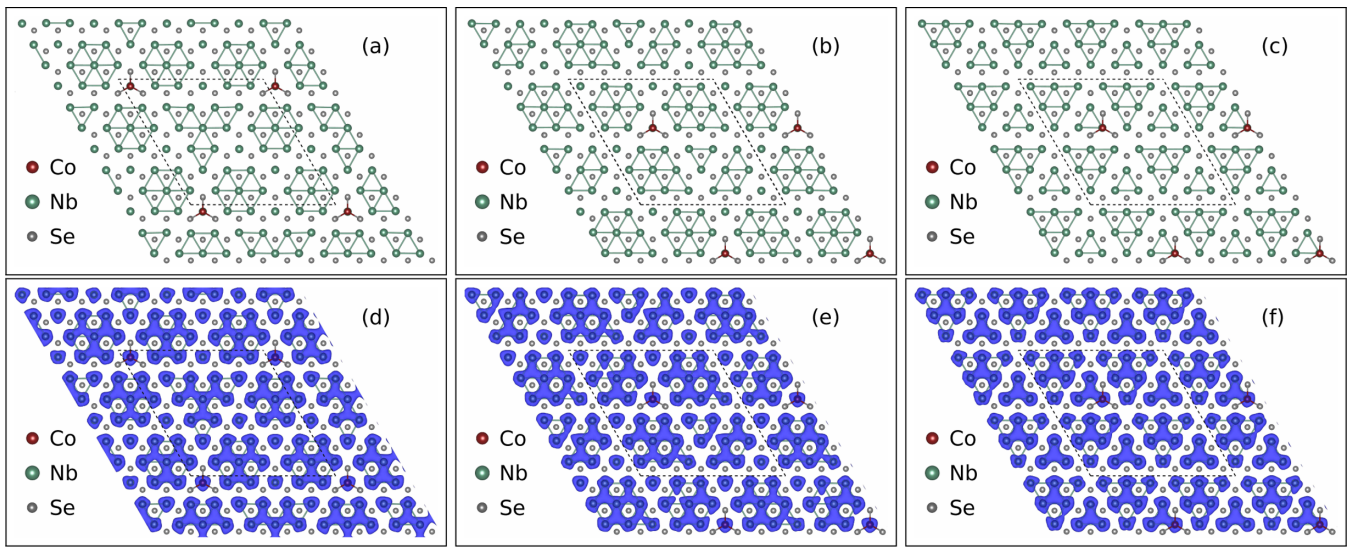

FIG. 3. First row: ground state Co|$NbSe_2$ HX-S (a), HX-A (b), and T-U (c) CDW structure. Second row: charge densities of the respective CDW structures. The isosurface value for the volumetric data is set in agreement with Fig. 1. Atoms are represented by spheres, as illustrated in the legends; Nb-Nb bonds shorter than the equilibrium distance (3.45 Å) are represented by solid lines, to help visualizing the CDW structure pattern. Dashed lines mark the supercells borders.

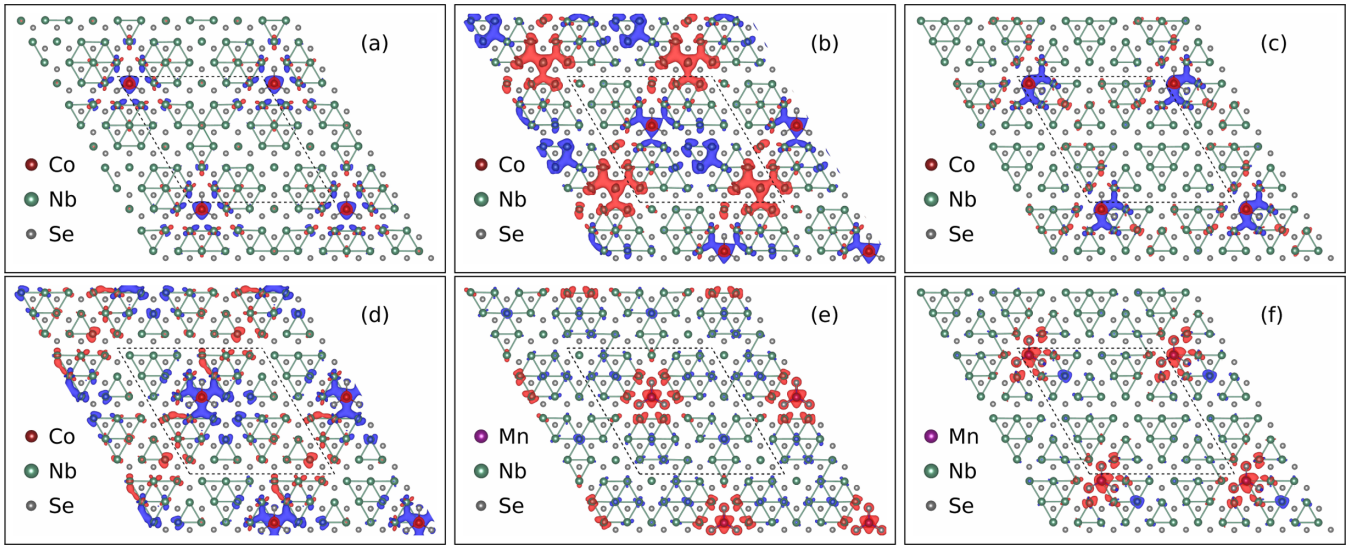

FIG. 4. Magnetization densities of Co|$NbSe_2$ HX-S (a), Co|$NbSe_2$ HX-A (b), Co|$NbSe_2$ T-U at 1 (c), Co|$NbSe_2$ T-U at 3 (d), Mn|$NbSe_2$ HX-A (e), and Mn|$NbSe_2$ T-U at 1 (f). The magnetization densities in (c) and (d) are different although they have virtually the same structure and total energy; the magnetization in (c) is juxtaposed to (f) to compare structures with the same adsorption site. Volumetric data are represented as blue (red) surfaces enclosing points whose magnetization density is greater than or equal to 0.0075 (smaller than or equal to −0.0075) μ_B/Bohr^3. Atoms are represented by spheres, as illustrated in the legends; Nb-Nb bonds shorter than the equilibrium distance (3.45 Å) are represented by solid lines to help visualizing the CDW structure pattern. Dashed lines mark the supercells borders.

The FT plots relative to Co|$NbSe_2$ HX-A, Co|$NbSe_2$ HX-S, and Mn|$NbSe_2$ HX-A are shown in Figs. 6(a)–6(c); the FTs shown are a computed difference with respect to the pristine T-U CDW. In these cases with adsorbates, a peak in the neighborhood of $|\mathbf{q}| = 0$ appears, because of the background charge (uniformly) injected into the system. All plots in Fig. 6 point to a considerable suppression (enhancement) of the CDW intensity along ΓM at $|\mathbf{q}| = 2\pi/3a$ (at $|\mathbf{q}| = \pi/a$); such suppression/enhancement is anisotropic for Co HX-A, being large along the line $\mathbf{k}_y = 0$ and small along the other two ΓM lines; the other cases are isotropic (Co HX-S) or virtually isotropic (Mn HX-A). Furthermore, large depletion of intensity at $|\mathbf{q}| = 4\pi/3a$ at K as well as at $|\mathbf{q}| = 2\pi/3a, 4\pi/3a$ along $\Gamma_1\Gamma_1'$, illustrates again the difference between the pristine HX CDW (T-C as well) and the pristine T-U CDW observed above. Finally, intensity enhancement occurs also within the small hexagon marking the 3×3 CDW peaks (but with no leading $\mathbf{q}$ vector), suggesting a competition between modulations with different wavelengths, as previously discussed [40,62]. Indeed, strain-induced modifications of the $\mathbf{q}$ vector were recently found [67]. In general, the asymmetric form of the CDW intensity (with respect to pristine T-U) suggests a connection with recently observed stripe phases [52,53,67] of which it could be a precursor. The character of the asymmetry in the adsorbates systems is further treated in the Appendix, with reference to Fig. 14.

B. Adsorption of Mn

In the case of Mn adsorption, magnetism plays a major role. A high magnetic moment, which correctly describes Mn, favors the Nb site more than in the case of Co adsorption (the energy difference between the Nb site and the hollow site is five times larger), compare their energy differences in Table I. The ordering of the CDW structures, assessed by total energy calculations, follows the same pattern as in

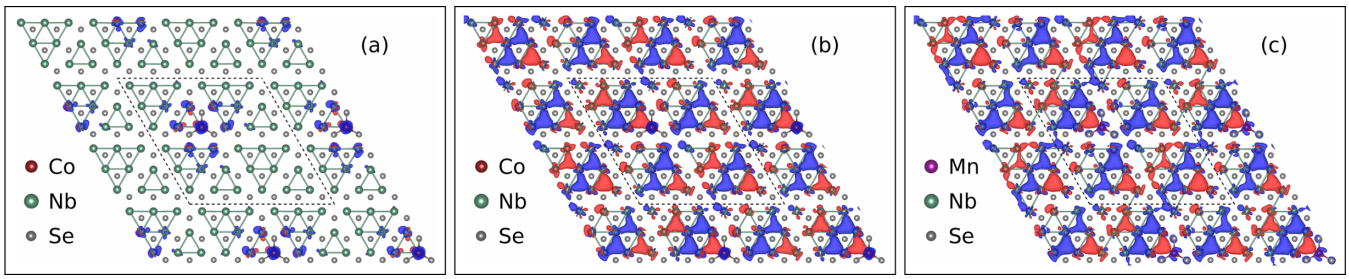

FIG. 5. Differences between charge density distributions. Co|$NbSe_2$ T-U minus $NbSe_2$ T-U (a), Co|$NbSe_2$ HX-A minus $NbSe_2$ T-U (b), and Mn|$NbSe_2$ HX-A minus $NbSe_2$ HX (c). Volumetric data are represented as blue (red) surfaces enclosing points whose electronic density is greater than or equal to 0.0025 (smaller than or equal to −0.0025) electrons/Bohr^3. Atoms are represented by spheres, as illustrated in the legends; Nb-Nb bonds shorter than the equilibrium distance (3.45 Å) are represented by solid lines to help visualizing the CDW structure pattern. Dashed lines mark the supercells borders.

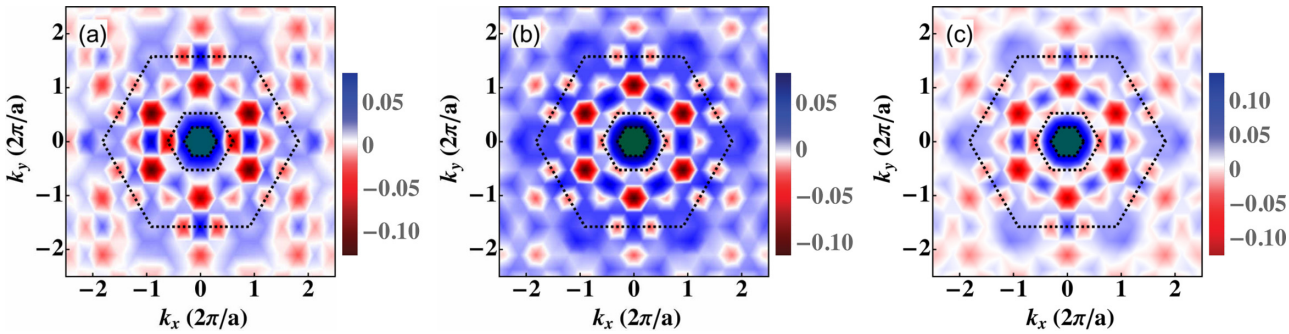

FIG. 6. Differences between FT of the charge density distribution of Co-adsorbed and Mn-adsorbed $NbSe_2$ CDWs and the T-U CDW in pristine $NbSe_2$. Ground state Co|$NbSe_2$ HX-A (a), Co|$NbSe_2$ HX-S (b), and Mn|$NbSe_2$ HX-A (c). The dashed hexagons mark the same regions as in Fig. 2 (see caption).

the case of Co adsorption, having a family of ground state HX CDWs, including a symmetric one and an asymmetric one, a solution of T-U at a higher energy and the absence of a T-C solution. The energy difference between the ground state HX CDW and the T-U solution is 1.5 meV/f.u., see Table II, which compared to the case of Co suggests that Mn drives a slightly stronger transition to a HX CDW. The charge density distributions of the HX-S and HX-A show no essential difference, being also very similar to that of Co|$NbSe_2$ HX-S. Therefore, the relative figures are omitted, and the remaining discussion is limited to the magnetization density distributions and the FT of the charge density distributions.

The magnetization densities of the HX-S, HX-A, and T-U are shown in Fig. 4, second row. The two HX CDWs are similar also in their magnetisation density distribution—compare with the case of Co adsorption, Fig. 4, second row. The structure of HX-A has a reflection symmetry through the top-left to bottom-right diagonal as represented in Fig. 4. The T-U CDW structure is modified slightly in the vicinity of the adsorption site. The magnetization density in all of the CDWs is negative around Mn, unlike the case of Co, where a negative cloud surrounding Co is neighbored by a positive cloud around the closest Nb atoms, compare also Figs. 17(a) and 17(b) in the Appendix, showing a detailed view on the vicinity of the adsorption sites.

TABLE III. Energetics and magnetism for M|$NbSe_2$ (M = Co, K, Ga, Mn). Energies are given as differences with respect to the lowest energy solution and are expressed in meV; magnetic moments are expressed in μ_B.

		μ^{TM}	μ_{tot}	E^{ad}
Co	T-U	1.9	2.0	3.440
	HX-A	1.9	2.0	3.504
	HX-S	1.9	1.9	3.504
Mn	T-U	4.4	4.4	2.472
	HX-A	4.4	4.4	2.559
	HX-S	4.4	4.3	2.561
K	T-Uh	0.0	0.0	3.045
	T-UN	0.0	0.0	3.038
	HX-S	0.0	0.1	3.060
Ga	T-U	0.0	0.0	2.907
	HX-A	0.0	0.0	2.946
	HX-S	0.0	0.0	2.944

Charge density differences in direct space are analyzed in comparison with Co adsorption. The main difference between the two adsorbates is that with Mn adsorption the out-of-plane charge modulations are not suppressed. In fact, note that the in-plane red lobes in Fig. 5(e) replace the out-of-plane red lobes in Fig. 5(c), point in three directions, symmetrically. In fact, the similarity between Figs. 5(d) and 5(f) confirms that the HX-S has the same features in the case of Co and Mn, with blue lobes pointing out of plane.

The analysis of the FT plots was mentioned previously with reference to Fig. 6. The main difference with the case of Co adsorption is that the HX-A and HX-S do not differ much, i.e., the intensity variation shows little contrast between the C_6 and the C_2 symmetries, compare the HX-A and HX-S CDWs in Figs. 6(c) and 14(c). The preference of the TM for the HX CDWs seems to be at variance with their tendency of reducing the symmetry from C_6 to C_2. The lowest energy solutions for Co|$NbSe_2$ (and Mn|$NbSe_2$) are mixed state of HX and T-C CDWs, compare Fig. 3(b) with Fig. 1(b). However the Co|$NbSe_2$ HX-A CDW solution has a consistent T-C component, whereas the Mn|$NbSe_2$ HX-A CDW solution has a small T-C component, see the underlying structure in the magnetization density plot, Fig. 4(e).

The CDW solutions for TM adsorbates on $NbSe_2$ are in fact mixed states; where the mixing between HX and T-C is high, the symmetry of the charge density distribution is reduced, whereas predominant HX CDW solutions keep a C_6 symmetry. In the case of Mn, the preference for HX solutions is higher than in the case of Co, and as a result the T-C component in the mixed solutions is smaller and in turn the C_6 symmetry is virtually maintained. Finally, the observation that the T-U/T-C have a reduced symmetry raises the question on pristine T-U/C and the symmetry of its charge density distribution, which has a C_6 symmetry; perhaps the adsorbates induce some symmetry breaking which allows the T-U to undergo a transition.

Table IV shows the occupancies of Co and Mn 3*d* orbitals. The environment around the TM in the $NbSe_2$ layer is trigonal prismatic, and therefore orbitals split into three groups due to the crystal field; these are classified according to their symmetry into e'', e', and a_1'. The orbital splitting is valid also for Co and Mn 3*d* orbitals, but the intensity of the splitting

TABLE IV. Occupancies on Co and Mn 3*d* orbitals, which split according to a trigonal prismatic environment, namely e'', e', and a_1', where $a_1' = d_{z^2-3r^2}$. The coefficients $u_\uparrow$, $v_\uparrow$, $u_\downarrow$, and $v_\downarrow$ are 0.90, 0.43, 0.62, and 0.78 for Co and 0.99, 0.16, 0.78, and 0.62 for Mn, respectively.

	Co		Mn	
	$\sigma =\uparrow$	$\sigma =\downarrow$	$\sigma =\uparrow$	$\sigma =\downarrow$
$e'_{l,\sigma}$	0.93	0.07	0.93	0.03
a'_l	0.90	0.79	0.92	0.08
$e''_{l,\sigma}$	0.95	0.92	0.93	0.09

is reduced because the environment is incomplete. Therefore, the spin splitting, which depends on the l character of the orbitals is larger than or comparable to the crystal field splitting, and orbitals are ordered by increasing energy as follows: In the majority spin channel, e'', e', and a_1'; in the minority spin channel the order of e' and a_1' is inverted. Furthermore, the orbital projections onto cubic (real spherical) harmonics (d_{xy}, d_{yz}, $d_{z^2-3r^2}$, d_{zx}, and $d_{x^2-y^2}$, ordered by increasing m value) are spin dependent. The orbitals of the eigenbasis can be written as $e''^1_\sigma = v_\sigma d_{xy} + u_\sigma d_{yz}$, $e''^2_\sigma = u_\sigma d_{zx} + v_\sigma d_{x^2-y^2}$, $e'^1_\sigma = u_\sigma d_{xy} + v_\sigma d_{yz}$, and $e'^2_\sigma = v_\sigma d_{zx} + u_\sigma d_{x^2-y^2}$. (Freedom in the choice of the basis set allows one to set $a_1' = d_{z^2-3r^2}$.) The l character of the $e''^\uparrow$ orbitals is close to 1 (i.e., the u values are larger than the v values); conversely, the $e'^\uparrow$ orbitals have a prevalent $l = 2$ character (v values are larger); overall, this fact holds for the $e''^\downarrow$ and $e'^\downarrow$ orbitals. In summary, TM adsorption favors HX CDW, weakening the CDW signals for the T-U and T-C CDWs, and the symmetry of the charge distribution is reduced from C_6 to C_2, especially in the case of Co, where mixing between HX and T-C occur. The modulation of the magnetic density is dependent on the symmetry of the charge distribution: the higher the symmetry, the weaker the modulation. Also, due to a weaker crystal field splitting, the orbital order of the 3*d* of Co and Mn in the two spin channels is different. Finally, a probe for Mn and Co is given in terms of l character of their electrons.

C. Adsorption of K and Ga

The adsorption of K is different from the other cases, since the energy difference between having an adatom at the hollow site or on top of a Nb site (see Table I) is small and therefore can be reversed by the presence of a CDW. This is, in fact, what happens. While on a nonmodulated $NbSe_2$ structure, the hollow site stands 4 meV above the Nb adsorption site, on the CDW modulated structures the hollow site becomes more favorable, of about 0.2 meV/f.u. (their respective ground states are compared). The solutions obtained starting from the T-C converge to mixed states between T-C itself and HX and they are found at a high energy, while the T-U CDW is still favored by 0.7 meV/f.u. over the HX CDW (the energy difference slightly changes with respect to the pristine case). The CDW structure and charge density distribution (in the T-U) on the hollow site (the ground state) and on the Nb site look very similar, see Fig. 7, and trace back to the pristine CDW ground state, compare Fig. 1. The CDW is slightly enhanced inside the hexagon delimiting the CDW peaks but without a leading **q**. The symmetry of the FT plot for K on the Nb (hollow) site is reduced from C_6 to C_2 at the points $\mathbf{q} = (\pm\pi/3a, \pi/\sqrt{3}a)$ [$\mathbf{q} = (\pm 2\pi/3a, 0)$], see Fig. 8; however, the intensity is one order of magnitude smaller than that of the Nb and Mn cases. Note also the difference with the T-C CDW, showing that the signal of K-adsorbed T-U on the hollow site is significantly enhanced with respect to pristine T-C at distinct **q** vectors, see Fig. 8(c).

The case of Ga is interesting in comparison with K because Ga has a fully occupied *s* shell and a single electron in the *p*

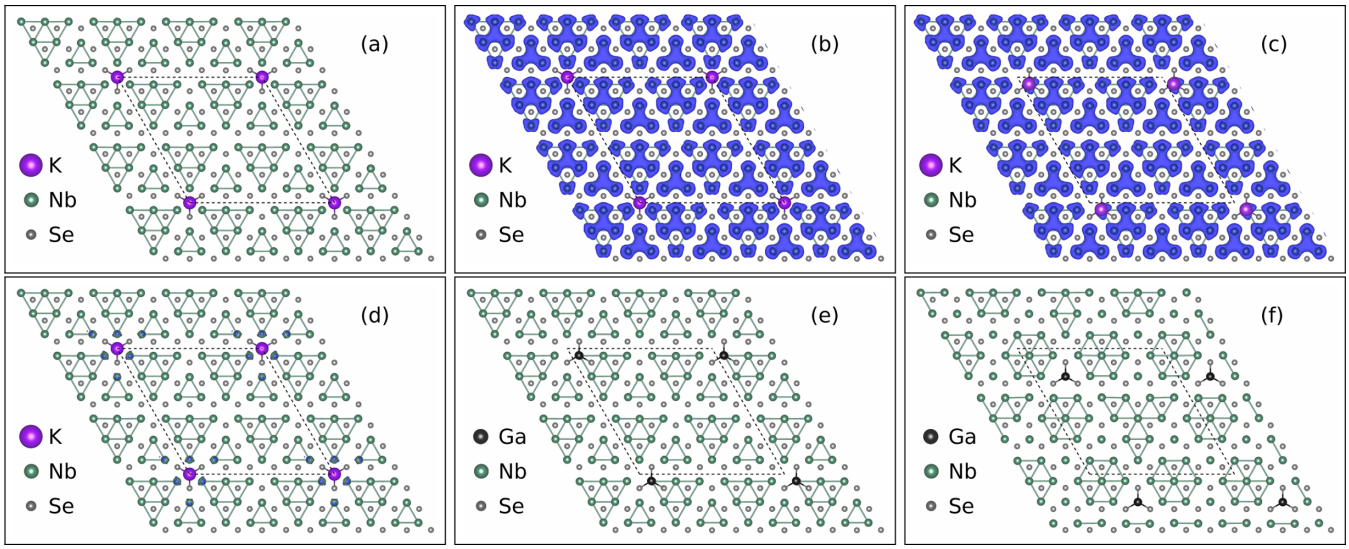

FIG. 7. First row: ground state CDW structure, with K adsorbed on the hollow position (a), its charge density distribution (b), and the charge density for K adsorbed on the Nb site (c). Second row: Difference in the charge densities between the K|$NbSe_2$ ground state and $NbSe_2$ T-U (d), ground state CDW structures for two Ga|$NbSe_2$, namely T-U (e) and HX-A (f). Atoms are represented by spheres, as illustrated in the legends; Nb-Nb bonds shorter than the equilibrium distance (3.45 Å) are represented by solid lines to help visualizing the CDW structure pattern. Dashed lines mark the supercells borders. The isosurface value for the volumetric data is set in agreement with Fig. 1.

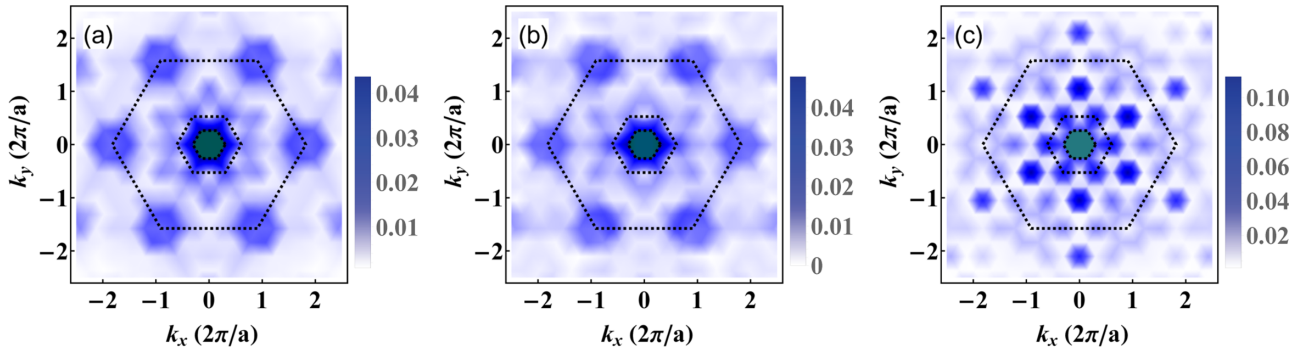

FIG. 8. Difference in the FT of the charge density distributions between the K|$NbSe_2$ on the hollow site (a), Nb site (b), and the T-U pristine CDW. The charge distribution has a C_2 symmetry for the adsorption on the hollow site and a C_6 symmetry for the adsorption on the Nb site. In (c), the FT difference between K|$NbSe_2$ on the hollow site and the pristine T-C CDW is shown.

shell. In this case, the adsorption on the Nb site is favored by 183 meV over the adsorption at the hollow site. The T-U CDW is in strong competition or coexists with the HX CDW, and the T-C converges to a mixed solution between T-C and HX, analogously to the case of K. The ground state structures are shown in Fig. 7. The charge density distributions and their FTs are not particularly different from the case with K adsorption. Both K and Ga cases are related to gate doping, because they consist of an electron per 36 f.u. injected in the system. However, structural reconstructions due to the chemical adsorption must be considered for the enhancement or suppression of the CDW order. Compared to experimental observations with gate doping [20], where the case of K and Ga adsorption suppress the CDW order, the FT plots suggest that a considerable order remains (no depletion is seen at any $\mathbf{q}_{CDW}$). Therefore, a doping with a hole carrying atom could enhance the CDW signal.

Overall, adsorption of atoms on single layers $NbSe_2$ suppresses the T-C CDW and promotes the HX CDWs in all cases; in particular, with Co and Mn the HX CDWs become the ground state for all the coverage considered in this study, whereas in the case of Ga the HX CDWs are at the same energy of the T-U CDW. Adsorption of K does not change the ground state (T-U) but does suppress the T-C CDW; the HX CDW solutions are the closest ones to the ground state (0.7 meV/f.u. above it), within thermal fluctuations, and therefore they are very likely to be seen by scanning tunnelling microscopy in real samples. In fact, as several STM data are becoming available, a guide on the CDW hierarchy may be very useful to correctly identify and locate metallic impurities in TMDCs.

A detailed comparison between theory and experiment requires also an analysis of the role of the substrate, which may induce a variety of effects, as, e.g., in-plane strain and charge transfer. Recently, single layers were grown on bilayer graphene, and a CDW order slightly weaker compared to the bulk was reported [19]; however, the phase competition between different modulations was not investigated. Our study suggests, based on the few examples analyzed, that one CDW phase (T-U) is suppressed with respect to other hidden ones (HX). As a concluding remark, we observe that the symmetry of the charge density distribution is reduced from C_6 to C_2, hinting at a weakening of a $\mathbf{q}$ vector, which may be the precursor of a stripe phase recently observed by STM [52,53].

V. CONCLUSIONS

By means of *ab initio* calculations based on total energy and direct space charge computation, we have investigated the existence and competition of CDWs in single-layer $NbSe_2$ without and with impurities. The T-C CDW is suppressed in all cases, suggesting that its observation in STM images is unlikely in nonpassivated samples, due to the high reactivity of $NbSe_2$ and, in general, metallic TMDCs. Transition metal adsorbates invert the energy hierarchy between CDWs, favoring the HX CDWs over the T-U and the T-C. Adsorption of K keep the T-U CDW as the ground state, although the HX CDW is preferred to the T-C CDW; adsorption of Ga equally

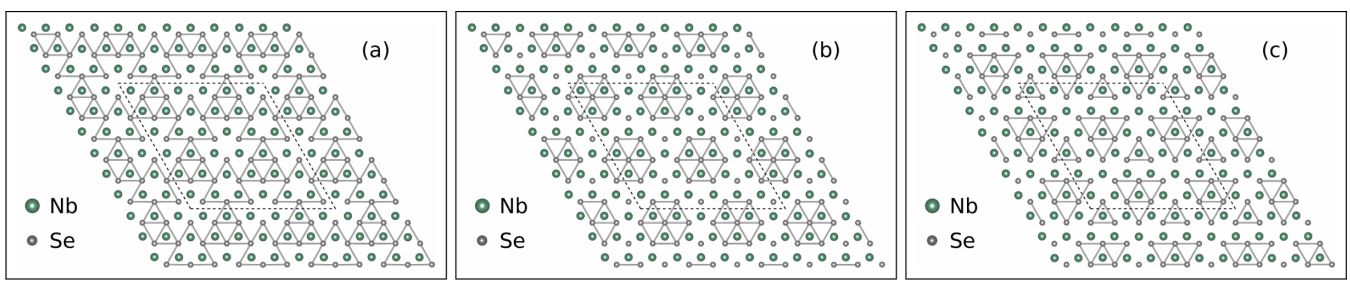

FIG. 9. Relaxed structures of the pristine CDWs as they appear in Fig. 1. 1 in the main text: T-U (a), T-C (b), and HX (c). Atoms are represented by spheres, as illustrated in the legends; Se-Se bonds shorter than the equilibrium distance (3.45 Å) are represented by solid lines, in order to help visualizing the CDW structure pattern. Dashed lines mark the supercells borders.

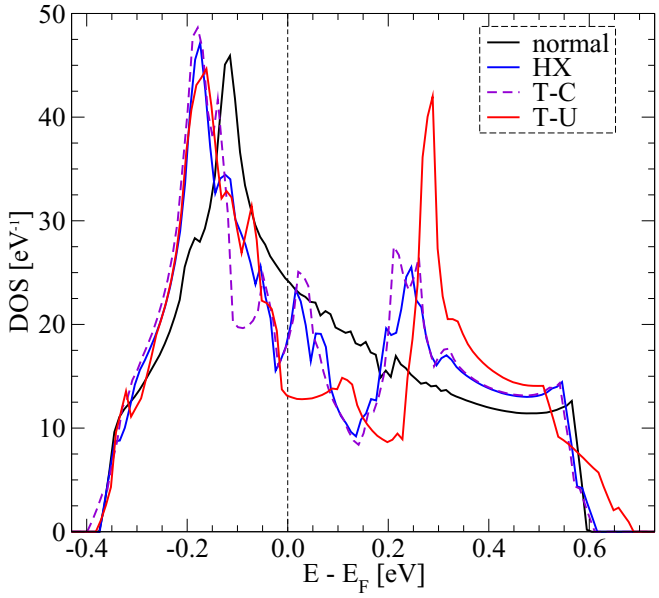

FIG. 10. Total DOS of $NbSe_2$ with the fully symmetric structure and with the HX, the T-C, and the T-U CDW structures, obtained for a $3 \times 3 \times 1$ supercell.

favors the T-U and the HX CDWs pointing to a coexistence. In general, adsorption of atoms changing the local symmetry mixes the 'pristine' CDWs, in particular the HX and the T-C. The symmetry of the charge density distribution is reduced from C_6 to C_2 upon Co or Mn adsorption. Future research will be focused on understanding the role of the substrate in the stabilization of the CDWs, in order to have a better correspondence between theory and experiment.

ACKNOWLEDGMENTS

We are grateful to B. I. Min, V. Fiorentini, E. Tosatti, and D. Payne for fruitful discussions. This research work was supported by the Ministry of Education, Gyeongsangbuk-do and Pohang City, through the National Research Foundation of Korea (Grants No. 2015R1C1A1A01052411, No. 2017R1D1A1B03033465, and No. 2016R1D1A1B02008461) as well as by the Institute for Basic Science (Grant No. IBS-R014-D1). K.K. and A.A. acknowledge the Max Planck POSTECH/KOREA Research Initiative programs through the National Foundation of Korea (NRF) funded by the Ministry of Science, ICT and Future Planning (Grant No. 2016K1A4A4A01922028). The computational work was performed on resources provided by the Swedish National Infrastructure for Computing (SNIC) at the High Performance Computing Center North (HPC2N), at the PDC center for High Performance Computing, and on the National Computational Infrastructure (NCI) of Australia. Further computational resources were provided by the IBS center at POSTECH and the Korean Institute of Science and Technology Information (KISTI).

APPENDIX A: PRISTINE

As reported in the literature, the (multidimensional) potential energy surface of the CDW phase features several (rather shallow) minima; as a result, several symmetries are possible. The existence of two forms of orthorhombically distorted structures was mentioned in the main text and is extensively explained in the literature. Some differences identified in the main text included the mention of the accompanying Se-Se bonds. Figures 9(a), 9(b) and 9(c) show the T-U, T-C, and HX CDWs, respectively, highlighting their Se-Se distance patterns. Also hexagonally distorted structures can exist in two forms, one having hexagonal Nb-Nb patterns, analyzed throughout the paper, and one having threefold symmetric Nb clusters, as shown in Fig. 12. This latter structure does not converge within our $6 \times 6 \times 1$ supercells and appears to be stabilized only in a $9 \times 9 \times 1$ supercell; it is found at a higher energy with respect to the other three CDW structures (2.7 meV above the T-U CDW structure) and therefore further analysis has been dismissed; Figs. 12(a) and 12(b) show its structure with its Nb clusters and its Se clusters, respectively.

With reference to Fig. 10, the DOS of the main three CDW structures are compared to the DOS of the fully symmetric structure of pristine $NbSe_2$. As presented elsewhere [40], for single layers a single band crosses the Fermi level and extends from ~ -0.4 eV to $\sim +0.7$ eV. As the main contribution for this band come from Nb states, we refer to such band as Nb band. The CDW formation shifts the spectral weight from ~ -0.10 eV to ~ -0.20 eV and enhances it in the range $(+0.25, +0.30)$ eV; the DOS peaks are aligned around -0.20 eV, whereas the DOS peaks around $+0.25$ eV are at

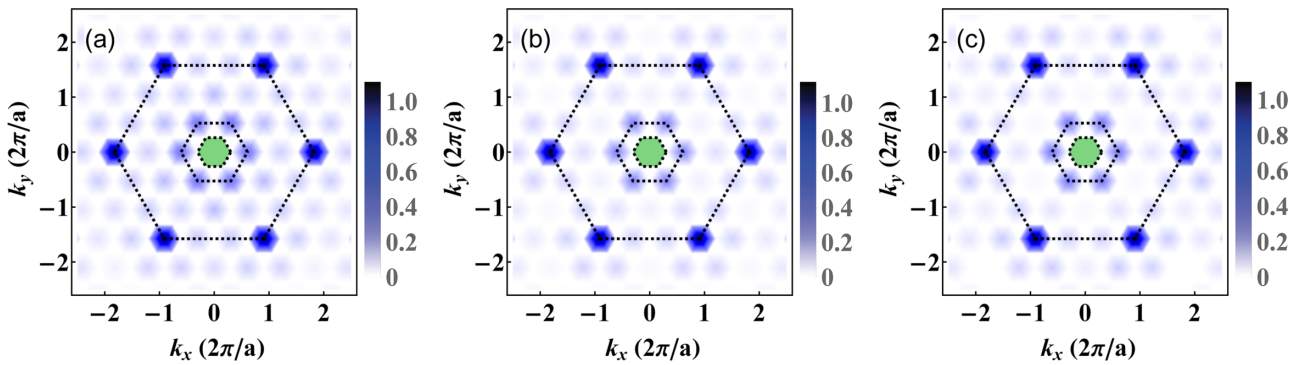

FIG. 11. Fourier transform (FT) plots of the charge density distributions for the pristine T-U (a), T-C (b), and HX (c) CDW structures, as given in Fig. 1. The dashed hexagons mark the same regions as in Fig. 2 (see caption).

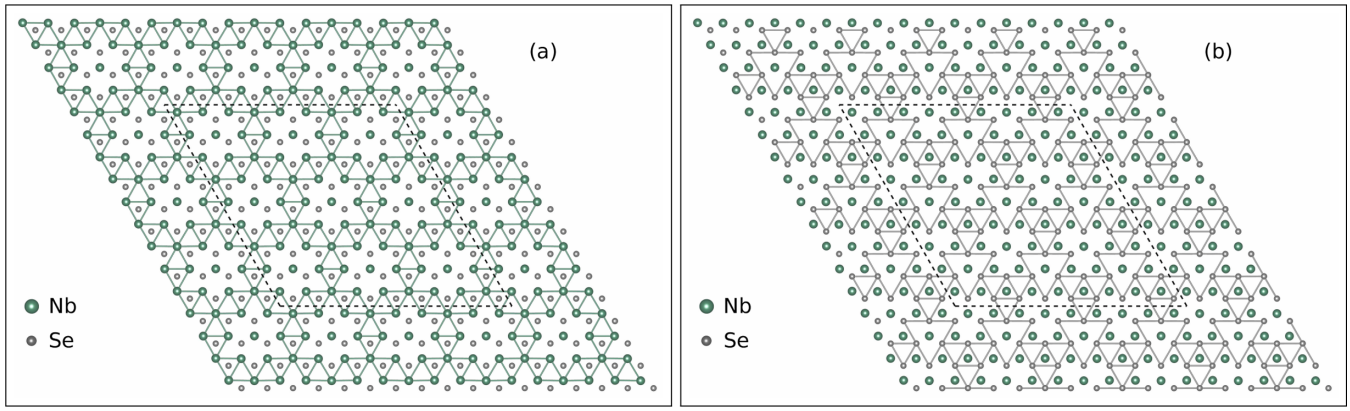

FIG. 12. Relaxed structures of a variant of the HX CDW in a $9 \times 9 \times 1$ supercell, highlighting its Nb-Nb (a) and Se-Se (b) distance pattern. Atoms are represented by spheres, as illustrated in the legends; in (a) and (b), respectively, Nb-Nb or Se-Se bonds shorter than the equilibrium distance (3.45 Å) are represented by solid lines, in order to help visualizing the CDW structure pattern. Dashed lines mark the supercells borders.

different energy for different CDWs. The T-U CDW DOS features a depletion of spectral weight in correspondence of the Fermi level until $\sim+0.10$ eV and a trough at $\sim+0.20$ eV (which in fact precedes the peak at $\sim+0.30$ eV); the T-C CDW DOS has a trough at ~-0.10 eV, a second one at Fermi level, and a third one at $\sim+0.15$ eV; the HX CDW DOS has one trough at Fermi level and one at $\sim+0.15$ eV, being more similar to the T-C CDW DOS. The T-U differs from the other two also by a slightly larger bandwidth, whose tail reaches $\sim$0.7 eV. Overall, the CDW affects different energy ranges of the DOS both around the Fermi level and away from it, in agreement with the literature [40,63].

APPENDIX B: CO ADSORPTION

The DOS of symmetric and selected CDW structures obtained in the $6 \times 6 \times 1$ supercells, computed and analysed for Co|$NbSe_2$ and for K|$NbSe_2$ in $6 \times 6 \times 1$ supercells, is shown in Fig. 13. By relaxing the M|$NbSe_2$ (M = Co, K) structures fixing the in-plane coordinates of the Nb and Se atoms, the symmetry of each structure was preserved; their relative DOS curves are labeled 'sym.' The main features of the DOS of the T-U and HX CDWs are maintained with respect to the pristine CDWs: the peaks at ~-0.20 eV and $\sim+0.25$ eV, and the depletion of states around the Fermi level. However, the position of the peaks for the HX-A and T-U CDWs are now different in the case of Co adsorption; also, while the depletion of states in the pristine HX CDW is accompanied by peaks and troughs near the Fermi level, the depletion of states in the HX-A CDW (i.e., with Co adsorbates) shows a profile in line with the T-U CDW. In summary, the effect of the CDW on the DOS slightly differs passing from the pristine case to the case with adsorbates, the states around the Fermi level being the most affected ones.

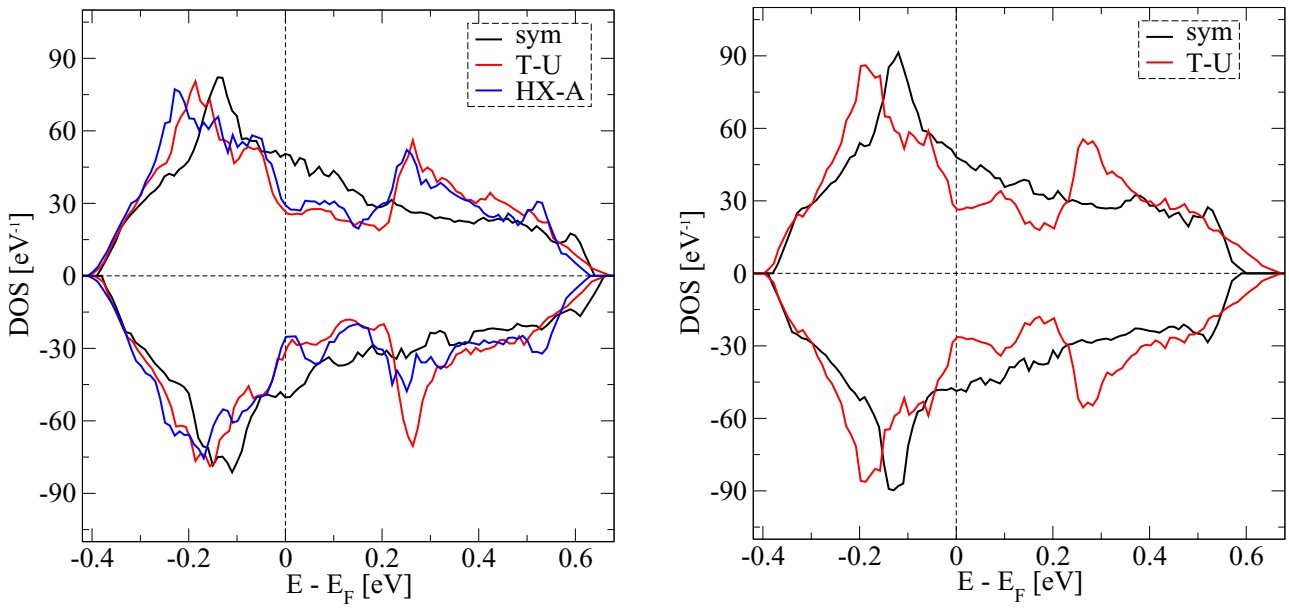

FIG. 13. Total DOS of Co|$NbSe_2$ and K|$NbSe_2$ with symmetric structures and with their CDW structures.

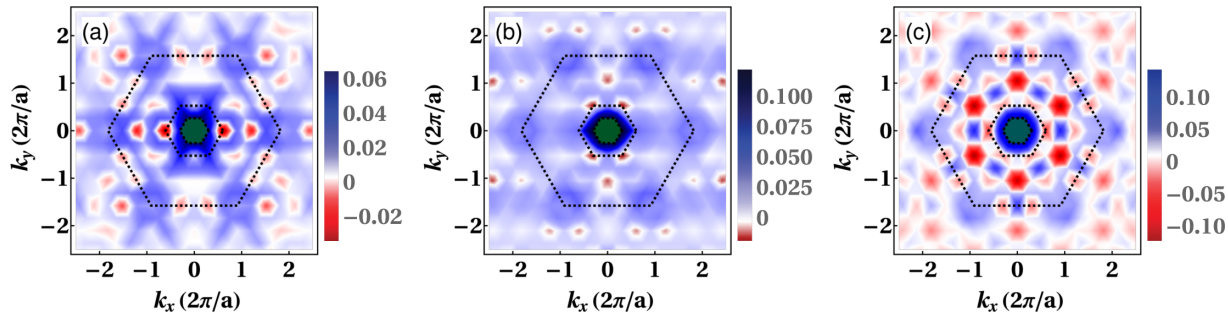

FIG. 14. Differences of the FT of the charge density distributions, done with respect to pristine T-U, of Co-adsorbed (a), Mn-adsorbed (b), T-U, and Mn-adsorbed (c) HX-S.

With reference to Fig. 14, we analyze further details of the effect of Co/Mn adsorption on the CDW intensity, started with Fig. 6. The asymmetry of the FT plots, highlighted by computing the difference with the charge distribution in the pristine CDWs (T-U in the case of Fig. 6) is clearly due to the adsorbate, rather than the asymmetric nature of the CDW itself. In fact, Figs. 14(a) and 14(b) show the FT of the charge densities of Co-adsorbed T-U and Mn-adsorbed T-U minus pristine T-U—while Fig. 14(c) shows the Mn HX-S minus pristine T-U for comparison with the figure in the main text. The effect of Co adsorption and Mn adsorption on the CDW peaks is somehow opposite to each other: Co adsorption suppresses the CDW at $\mathbf{q} = (\pm 2\pi/3a, 0), (\pm 4\pi/3a, 0)$ while enhancing it along the lines $\mathbf{q} = (\pm\pi/a, \sqrt{3}\pi/a)$; Mn adsorption suppresses the CDW at $\mathbf{q} = (\pm\pi/3a, \pi/\sqrt{3}a), (0, 2\pi/\sqrt{3}a)$, enhancing it only at small values of $|\mathbf{q}|$. The asymmetry of the charge distribution of T-U suggests that such asymmetry is still reduced even for low concentrations of Co/Mn, when the energy competition starts to turn in favor of the T-U CDW.

A single Co adsorbed on $NbSe_2$, with a concentration of 1 atom over 81 unit cells (a $9 \times 9 \times 1$ replica), was studied in order to assess how fast the energy order changes to recover that of pristine system. Four solutions were found within 0.4 meV/f.u, see Fig. 15; such a small difference in energy makes them accessible by thermal fluctuations. The structure of the HX solutions shows some similarities to the case with higher adsorbate coverage. Among the low energy solutions, the T-C CDW was found with some mixing with HX and

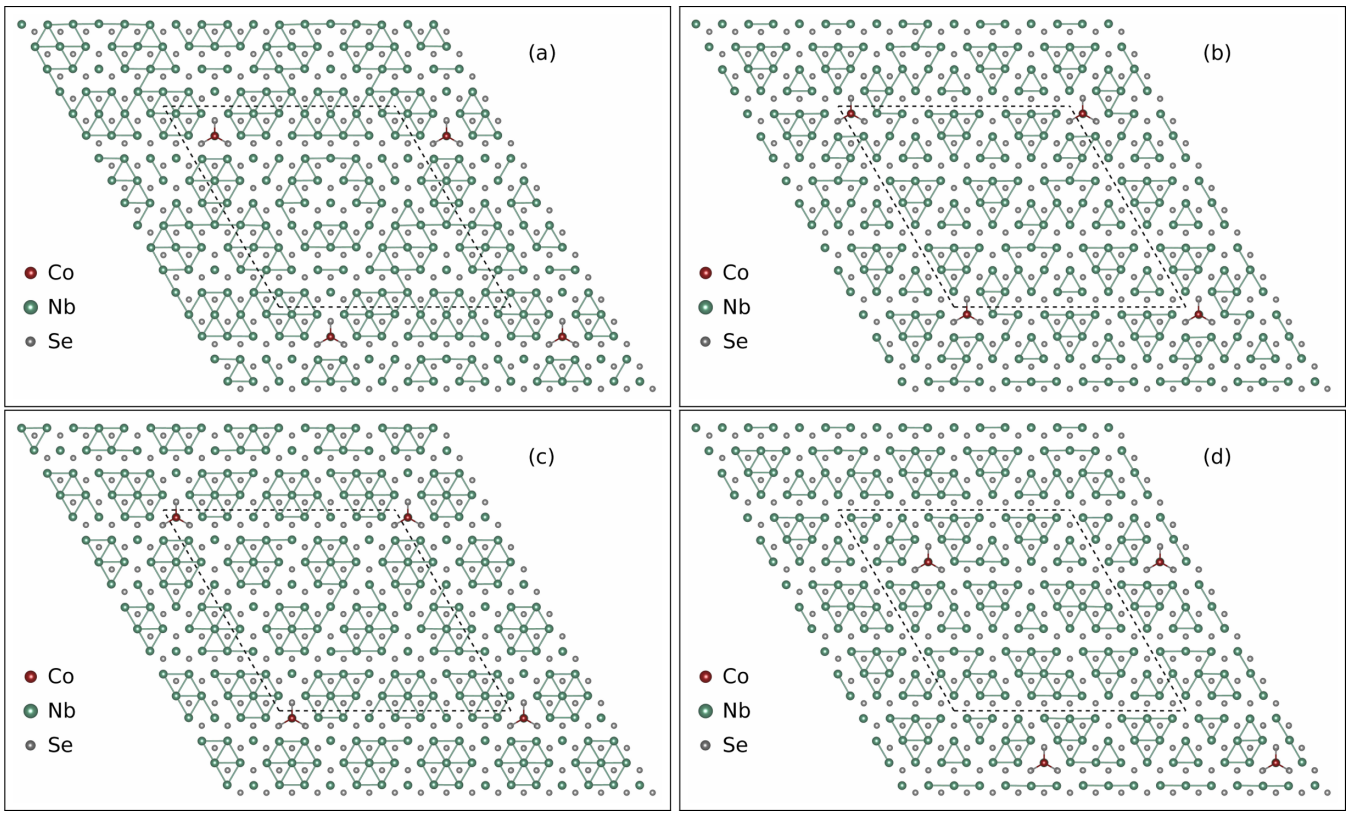

FIG. 15. Relaxed structures of Co|$NbSe_2$ in a $9 \times 9 \times 1$ supercell. Atoms are represented by spheres, as illustrated in the legends; Nb-Nb bonds shorter than the equilibrium distance (3.45 Å) are represented by solid lines, in order to help visualizing the CDW structure pattern. Dashed lines mark the supercells borders.

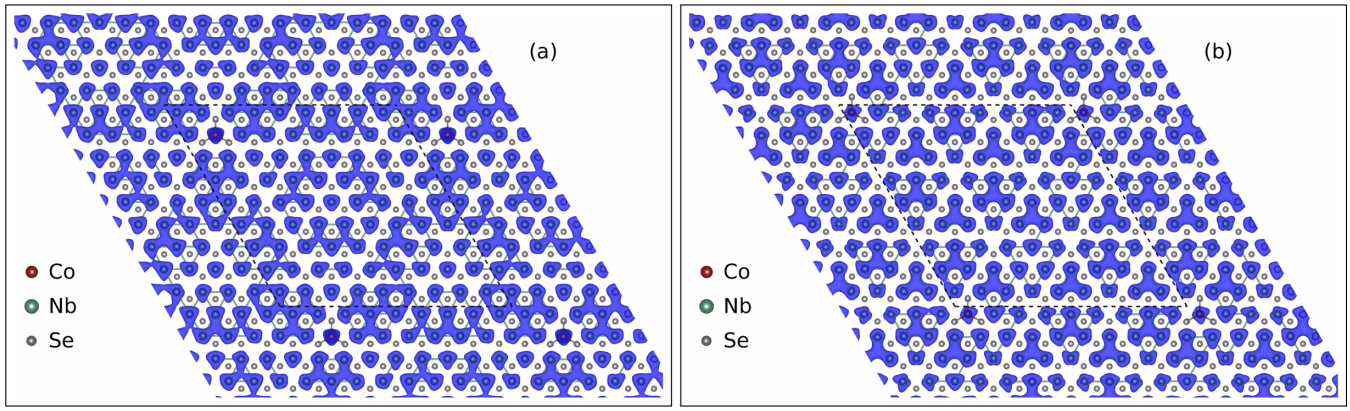

FIG. 16. Direct space charge density distribution of Co|$NbSe_2$ in a $9 \times 9 \times 1$ supercell; (a) and (b) correspond to the respective structures in Fig. 15. The isosurface value for the volumetric data is set in agreement with the relative figures in the main text. Atoms are represented by spheres, as illustrated in the legends; Nb-Nb bonds shorter than the equilibrium distance (3.45 Å) are represented by solid lines, in order to help visualizing the CDW structure pattern. Dashed lines mark the supercells borders.

T-U, see Figs. 15(a), 15(c) and 15(d). The T-U solutions are closer in energy to the ground state solution HX-A (0.3–0.4 meV/f.u.), whereas other mixed structures are found at higher energy, Figs. 15(b) and 15(d), respectively.

The direct space charge distributions of the lowest energy HX solution and the first T-U solution are shown in Figs. 16(a) and 16(b), corresponding to the structures shown in Figs. 15(a) and 15(b); the HX solution shows characteristic patches of the T-C and HX CDWs, following the structural modulation and confirming the tendency for these two CDW to mix together upon Co adsorption; in fact, patches as represented in Fig. 1 are found in the $9 \times 9 \times 1$ supercell. The charge distribution of the T-U solution looks almost identical to that in the $6 \times 6 \times 1$ supercell, including the reduced symmetry, which is likely due to unidirectional local structural distortions driven by the Co electronic degree of freedom.

Finally, the energetic stability of CDWs in Co|$NbSe_2$ was also used to estimate how small changes of U and J affect the results presented in this paper. Several DFT+U calculations were performed for the $6 \times 6 \times 1$ supercell, sampling U in the range 3–5 eV and J in the range 0.5–0.9 eV. We found that the values reported in Table II are independent from the chosen Coulomb interaction parameters. The only exception is the calculation for $U = 5$ eV and $J = 0.5$ eV, when the HX-A CDW ends up in a different solution (minimum), much higher in energy, while the other two CDWs keep their energetic arrangement.

APPENDIX C: MAGNETIC DENSITY

The comparison between magnetic couplings within the Nb band in the two cases of Co adsorption and Mn adsorption has been discussed in the main text. The actual magnetic moments (i.e., involving all states up to the Fermi level) of Co, Mn, and their respective underlying Nb atoms are $+1.9\ \mu_B$, $+4.4\ \mu_B$, $+0.6\ \mu_B$, and $-0.8\ \mu_B$, respectively. In summary, the Co and Mn magnetic moments in the Nb bands are inverted with respect to the total magnetic moments, while the underlying Nb magnetic moments do not change sign, remaining positive in the case of Co adsorption and negative in the case of Mn adsorption.

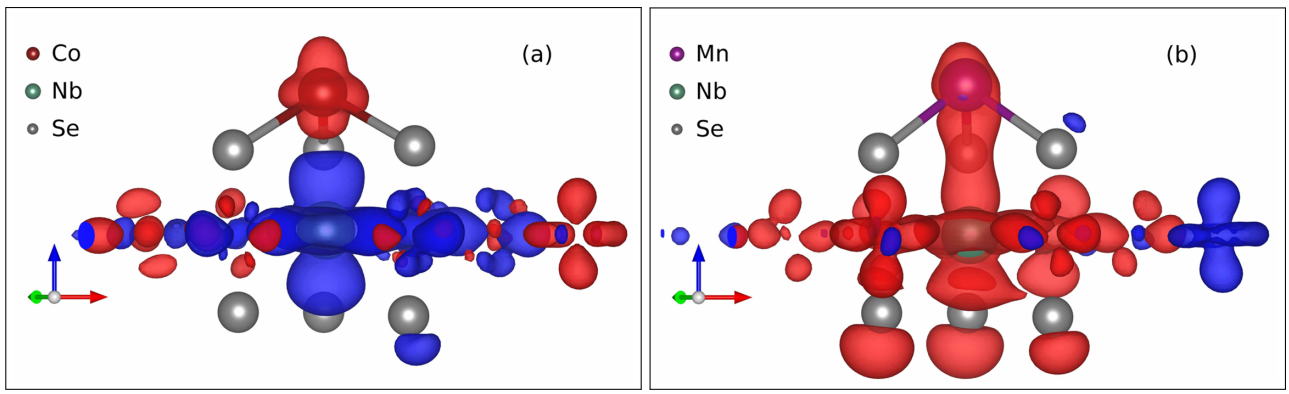

FIG. 17. Magnetization densities of Co|$NbSe_2$ T-U (a) and Mn|$NbSe_2$ T-U (b) with details around Co and Mn, respectively. The sets of axes represent the unitary lattice vectors in red, green, and blue color, respectively. Volumetric data representation is set in agreement to the relative figures in the main text.

[1] K. S. Novoselov, D. Jiang, F. Schedin, T. J. Booth, V. V. Khotkevich, S. V. Morozov, and A. K. Geim, Proc. Natl. Acad. Sci. USA **102**, 10451 (2005).

[2] M. Xu, T. Liang, M. Shi, and H. Chen, Chem. Rev. **113**, 3766 (2013).

[3] W. Choi, N. Choudhary, G. H. Han, J. Park, D. Akinwande, and Y. H. Lee, Mater. Today **20**, 116 (2017).

[4] S. Z. Butler, S. M. Hollen, L. Cao, Y. Cui, J. A. Gupta, H. R. Gutiérrez, T. F. Heinz, S. S. Hong, J. Huang, A. F. Ismach, E. Johnston-Halperin, M. Kuno, V. V. Plashnitsa, R. D. Robinson, R. S. Ruoff, S. Salahuddin, J. Shan, L. Shi, M. G. Spencer, M. Terrones, W. Windl, and J. E. Goldberger, ACS Nano **7**, 2898 (2013).

[5] A. K. Geim and I. V. Grigorieva, Nature (London) **499**, 419 (2013).

[6] K. S. Novoselov, A. Mishchenko, A. Carvalho, and A. H. Castro Neto, Science **353**, aac9439 (2016).

[7] A. Splendiani, L. Sun, Y. Zhang, T. Li, J. Kim, C.-Y. Chim, G. Galli, and F. Wang, Nano Lett. **10**, 1271 (2010).

[8] K. F. Mak, C. Lee, J. Hone, J. Shan, and T. F. Heinz, Phys. Rev. Lett. **105**, 136805 (2010).

[9] A. Kuc, N. Zibouche, and T. Heine, Phys. Rev. B **83**, 245213 (2011).

[10] Q. H. Wang, K. Kalantar-Zadeh, A. Kis, J. N. Coleman, and M. S. Strano, Nat. Nanotech. **7**, 699 (2012).

[11] M. Chhowalla, H. S. Shin, G. Eda, L.-J. Li, K. P. Loh, and H. Zhang, Nat. Chem. **5**, 263 (2013).

[12] R. F. Frindt, Phys. Rev. Lett. **28**, 299 (1972).

[13] J. A. Wilson, F. J. D. Salvo, and S. Mahajan, Adv. Phys. **50**, 1171 (2001).

[14] Z. R. Gong, W. Z. Luo, Z. F. Jiang, and H. C. Fu, Sci. Rep. **7**, 42390 (2017).

[15] Y. Qi, P. G. Naumov, M. N. Ali, C. R. Rajamathi, W. Schnelle, O. Barkalov, M. Hanfland, S.-C. Wu, C. Shekhar, Y. Sun, V. Süß, M. Schmidt, U. Schwarz, E. Pippel, P. Werner, R. Hillebrand, T. Förster, E. Kampert, S. Parkin, R. J. Cava, C. Felser, B. Yan, and S. A. Medvedev, Nat. Commun. **7**, 11038 (2016).

[16] J. M. Lu, O. Zheliuk, I. Leermakers, N. F. Q. Yuan, U. Zeitler, K. T. Law, and J. T. Ye, Science **350**, 1353 (2015).

[17] X. Xi, L. Zhao, Z. Wang, H. Berger, L. Forró, J. Shan, and K. F. Mak, Nat. Nanotech. **10**, 765 (2015).

[18] X. Xi, Z. Wang, W. Zhao, J.-H. Park, K. T. Law, H. Berger, L. Forró, J. Shan, and K. F. Mak, Nat. Phys. **12**, 139 (2016).

[19] M. M. Ugeda, A. J. Bradley, Y. Zhang, S. Onishi, Y. Chen, W. Ruan, C. Ojeda-Aristizabal, H. Ryu, M. T. Edmonds, H.-Z. Tsai, A. Riss, S.-K. Mo, D. Lee, A. Zettl, Z. Hussain, Z.-X. Shen, and M. F. Crommie, Nat. Phys. **12**, 92 (2016).

[20] X. Xi, H. Berger, L. Forró, J. Shan, and K. F. Mak, Phys. Rev. Lett. **117**, 106801 (2016).

[21] X. Zhu, Y. Guo, H. Cheng, J. Dai, X. An, J. Zhao, K. Tian, S. Wei, X. Cheng Zeng, C. Wu, and Y. Xie, Nat. Commun. **7**, 11210 (2016).

[22] A. J. Bevolo and H. R. Shanks, J. Appl. Phys. **45**, 4644 (1974).

[23] R. Corcoran, P. Meeson, Y. Onuki, P. A. Probst, M. Springford, K. Takita, H. Harima, G. Y. Guo, and B. L. Gyorffy, J. Phys.: Condens. Matter **6**, 4479 (1994).

[24] J. A. Wilson, F. J. Di Salvo, and S. Mahajan, Phys. Rev. Lett. **32**, 882 (1974).

[25] D. E. Moncton, J. D. Axe, and F. J. DiSalvo, Phys. Rev. Lett. **34**, 734 (1975).

[26] E. Revolinsky, G. A. Spiering, and D. J. Beerntsen, J. Phys. Chem. Solids **26**, 1029 (1965).

[27] D. J. Rahn, S. Hellmann, M. Kalläne, C. Sohrt, T. K. Kim, L. Kipp, and K. Rossnagel, Phys. Rev. B **85**, 224532 (2012).

[28] A. H. Castro Neto, Phys. Rev. Lett. **86**, 4382 (2001).

[29] J. A. Galvis, E. Herrera, C. Berthod, S. Vieira, I. Guillamón, and H. Suderow, Commun. Phys. **1**, 30 (2018).

[30] F. Zheng, Z. Zhou, X. Liu, and J. Feng, Phys. Rev. B **97**, 081101 (2018).

[31] C. J. Arguello, S. P. Chockalingam, E. P. Rosenthal, L. Zhao, C. Gutiérrez, J. H. Kang, W. C. Chung, R. M. Fernandes, S. Jia, A. J. Millis, R. J. Cava, and A. N. Pasupathy, Phys. Rev. B **89**, 235115 (2014).

[32] T. M. Rice and G. K. Scott, Phys. Rev. Lett. **35**, 120 (1975).

[33] R. Liu, C. G. Olson, W. C. Tonjes, and R. F. Frindt, Phys. Rev. Lett. **80**, 5762 (1998).

[34] T. Straub, T. Finteis, R. Claessen, P. Steiner, S. Hüfner, P. Blaha, C. S. Oglesby, and E. Bucher, Phys. Rev. Lett. **82**, 4504 (1999).

[35] D. S. Inosov, V. B. Zabolotnyy, D. V. Evtushinsky, A. A. Kordyuk, B. Büchner, R. Follath, H. Berger, and S. V. Borisenko, New J. Phys. **10**, 125027 (2008).

[36] K. Rossnagel, O. Seifarth, L. Kipp, M. Skibowski, D. Voß, P. Krüger, A. Mazur, and J. Pollmann, Phys. Rev. B **64**, 235119 (2001).

[37] K. Rossnagel and N. V. Smith, Phys. Rev. B **76**, 073102 (2007).

[38] M. D. Johannes, I. I. Mazin, and C. A. Howells, Phys. Rev. B **73**, 205102 (2006).

[39] M. D. Johannes and I. I. Mazin, Phys. Rev. B **77**, 165135 (2008).

[40] M. Calandra, I. I. Mazin, and F. Mauri, Phys. Rev. B **80**, 241108 (2009).

[41] T. Valla, A. V. Fedorov, P. D. Johnson, P.-A. Glans, C. McGuinness, K. E. Smith, E. Y. Andrei, and H. Berger, Phys. Rev. Lett. **92**, 086401 (2004).

[42] X. Zhu, Y. Cao, J. Zhang, E. W. Plummer, and J. Guo, Proc. Natl. Acad. Sci. USA **112**, 2367 (2015).

[43] C. J. Arguello, E. P. Rosenthal, E. F. Andrade, W. Jin, P. C. Yeh, N. Zaki, S. Jia, R. J. Cava, R. M. Fernandes, A. J. Millis, T. Valla, R. M. Osgood, and A. N. Pasupathy, Phys. Rev. Lett. **114**, 037001 (2015).

[44] V. N. Kotov, B. Uchoa, V. M. Pereira, F. Guinea, and A. H. Castro Neto, Rev. Mod. Phys. **84**, 1067 (2012).

[45] F. Guinea, M. I. Katsnelson, and T. O. Wehling, Ann. Phys. **526**, A81 (2014).

[46] K. F. Mak, K. He, C. Lee, G. H. Lee, J. Hone, T. F. Heinz, and J. Shan, Nat. Mater. **12**, 207 (2012).

[47] A. Skripov and A. Stepanov, Solid State Commun. **53**, 469 (1985).

[48] C. D. Malliakas and M. G. Kanatzidis, J. Am. Chem. Soc. **135**, 1719 (2013).

[49] J. Ángel Silva-Guillén, P. Ordejón, F. Guinea, and E. Canadell, 2D Materials **3**, 035028 (2016).

[50] U. Chatterjee, J. Zhao, M. Iavarone, R. Di Capua, J. P. Castellan, G. Karapetrov, C. D. Malliakas, M. G. Kanatzidis, H. Claus, J. P. C. Ruff, F. Weber, J. van Wezel, J. C. Campuzano, R. Osborn, M. Randeria, N. Trivedi, M. R. Norman, and S. Rosenkranz, Nat. Commun. **6**, 6313 (2015).

[51] C.-S. Lian, C. Si, J. Wu, and W. Duan, Phys. Rev. B **96**, 235426 (2017).

[52] A. Fang, C. Adamo, S. Jia, R. J. Cava, S.-C. Wu, C. Felser, and A. Kapitulnik, Sci. Adv. **4**, eaaq0330 (2018).
[53] A. Soumyanarayanan, M. M. Yee, Y. He, J. van Wezel, D. J. Rahn, K. Rossnagel, E. W. Hudson, M. R. Norman, and J. E. Hoffman, Proc. Natl. Acad. Sci. USA **110**, 1623 (2013).
[54] K. Cho, M. Konczykowski, S. Teknowijoyo, M. A. Tanatar, J. Guss, P. B. Gartin, J. M. Wilde, A. Kreyssig, R. J. McQueeney, A. I. Goldman, V. Mishra, P. J. Hirschfeld, and R. Prozorov, Nat. Commun. **9**, 2796 (2018).
[55] P. E. Blöchl, Phys. Rev. B **50**, 17953 (1994).
[56] G. Kresse and D. Joubert, Phys. Rev. B **59**, 1758 (1999).
[57] J. P. Perdew, K. Burke, and M. Ernzerhof, Phys. Rev. Lett. **77**, 3865 (1996).
[58] J. P. Perdew, K. Burke, and M. Ernzerhof, Phys. Rev. Lett. **78**, 1396 (1997).
[59] T. O. Wehling, A. I. Lichtenstein, and M. I. Katsnelson, Phys. Rev. B **84**, 235110 (2011).
[60] A. I. Liechtenstein, V. I. Anisimov, and J. Zaanen, Phys. Rev. B **52**, R5467 (1995).
[61] J. Wilson and A. Yoffe, Adv. Phys. **18**, 193 (1969).
[62] C.-S. Lian, C. Si, and W. Duan, Nano Lett. **18**, 2924 (2018).
[63] D. W. Shen, B. P. Xie, J. F. Zhao, L. X. Yang, L. Fang, J. Shi, R. H. He, D. H. Lu, H. H. Wen, and D. L. Feng, Phys. Rev. Lett. **99**, 216404 (2007).
[64] X. Wei, B. Zhao, J. Zhang, Y. Xue, Y. Li, and Z. Yang, Phys. Rev. B **95**, 075419 (2017).
[65] S. Kezilebieke, M. Dvorak, T. Ojanen, and P. Liljeroth, Nano Lett. **18**, 2311 (2018).
[66] Y. Zhou, Z. Wang, P. Yang, X. Zu, L. Yang, X. Sun, and F. Gao, ACS Nano **6**, 9727 (2012).
[67] S. Gao, F. Flicker, R. Sankar, H. Zhao, Z. Ren, B. Rachmilowitz, S. Balachandar, F. Chou, K. S. Burch, Z. Wang, J. van Wezel, and I. Zeljkovic, Proc. Natl. Acad. Sci. USA **115**, 6986 (2018).